

This document is the Accepted Manuscript version of a Published Work that appeared in final form in ACS Applied Energy Materials, copyright © 2019 American Chemical Society after peer review and technical editing by the publisher. To access the final edited and published work see <https://doi.org/10.1021/acsaem.9b01790>.

Pseudo-cubic Phase Tungsten Oxide as a Photocatalyst for Hydro-gen Evolution Reaction

Xiandi Zhang,[†] Wei Hao,[§] Chui-Shan Tsang,[†] Mengjie Liu,[†] Gyeong S. Hwang,^{,§} and Lawrence Yoon Suk Lee^{*,†}*

[†] Department of Applied Biology and Chemical Technology and the State Key Laboratory of Chemical Biology and Drug Discovery, The Hong Kong Polytechnic University, Hung Hom, Kowloon, Hong Kong SAR

[§] McKetta Department of Chemical Engineering, University of Texas, Austin, Texas 78712, United States

Keywords: tungsten oxide; phase transition; oxygen vacancy; photocatalytic hydrogen evolution; band structure engineering

Abstracts

Defect and phase engineering can effectively tune the activity of photocatalysts by altering their band structure and active site configuration. Herein, we report the phase-controlled synthesis of tungsten oxide (WO₃) nanoplates *via* wet-chemical approach. By adjusting the ratio of trioctylphosphine and trioctylphosphine oxide, oxygen vacancies are induced in WO₃ at a relatively low temperature, accompanying the crystal structure transition from monoclinic to

orthorhombic or pseudo-cubic phase. The experimental results and DFT calculations reveal that the increased oxygen vacant sites in WO_3 lead to the upshift in both conduction band minimum and valence band maximum. The reformed band structure of reduced WO_3 samples (WO_{3-x}) enables the photocatalytic hydrogen evolution without co-catalyst at a maximum steady rate of $340 \mu\text{mol g}^{-1} \text{h}^{-1}$ under simulated sunlight. Our work demonstrates a simple and effective strategy of introducing oxygen vacancy to WO_3 for band structure tuning, which may be further extended to other metal oxide systems.

Introduction

With the advantages in natural abundance, chemical stability, and low cost, transition metal oxides have been widely engaged in the development of energy conversion and storage devices.¹ Among them, tungsten trioxide (WO_3), a *n*-type semiconductor metal oxide, is particularly attractive for photocatalytic water splitting owing to the additional advantages of wide absorption of solar spectrum (*ca.* 12%) and good conductivity.² Nonetheless, restricted by its intrinsic band structure, WO_3 as standalone³ or hybridized with other semiconductors⁴⁻⁷ is only applicable to oxidation part of water splitting. The position of valence band maximum (VBM) of WO_3 is located at a relatively high energy level (3.0 eV vs. reversible hydrogen electrode, RHE), while the conduction band minimum (CBM) lies at a position lower than the hydrogen reduction potential (0 V vs. RHE), which forbids the photoreduction of water to hydrogen.

There have been much efforts to override such innate limitations by tuning the work function of semiconductors.⁸⁻¹⁰ For transition metal oxides, the oxygen vacancies (V_{Os}) introduced as controlled defect sites have been utilized to regulate the electronic structure and thus the work function of the material.^{11, 12} It is generally accepted that the elaborated control of type and population of V_{O} on metal oxides not only serves as a photo-induced charge trap that facilitates the separation and migration of electron-hole pairs^{13, 14} but also alters the band structure of metal oxides, thus promotes the photocatalytic activity.^{11, 15, 16} Recent studies on the V_{Os} -engineered WO_3 (WO_{3-x}) demonstrated that the V_{Os} can facilitate the charge transfer between WO_{3-x} and electrode, enhance the charge separation efficiency, and improve the surface adsorptivity of reactant, thereby leading to a significant improvement in sensing,¹⁷ photocatalytic oxygen evolution reaction (OER)¹⁸⁻²¹ and dye degradation,²² electrocatalytic hydrogen evolution reaction (HER),²³⁻²⁵ and alkene hydrogenation.²⁶ In addition, the introduction of V_{Os} to WO_3 has been

reported to upshift the VBM, which led to the promotion of the light harvest and the efficiency toward photocatalytic OER.²⁷ Xi et al. reported that the V_O-rich W₁₈O₄₉ nanowires can photocatalyze the reduction of CO₂ to CH₄.²⁸ Recently, our group also showed that the surface disordered layer enables WO₃ nanoplates to carry out photocatalytic HER without co-catalysts.²⁹ Nevertheless, it is still challenging to reconstruct the band structure and effectively upshift the CBM for photocatalytic HER without compromising the structural integrity.

In addition to the defect sites, the crystal phase plays another key role in determining the electronic structure of nanomaterials. This also leads to the altered photo- or electrocatalytic properties, as known for the cases of MoS₂³⁰ and TiO₂.³¹ The hexagonal 2H phase of MoS₂ is semiconducting and shows poor electrocatalytic activity towards HER, while the metastable metallic 1T phase shows a dramatically enhanced HER catalytic performance.^{30, 32} It is also well known that three polymorphs of TiO₂, namely, rutile, anatase, and brookite phases exhibit different photocatalytic HER activities and a better activity is reported when different polymorphs coexist.³³ Nickel phosphide is another good example displaying a phase-dependent electrocatalytic property. Among the HER active phases (Ni₁₂P₅, Ni₂P, and Ni₅P₄), the higher positive charge on Ni and a stronger ensemble effect of P endow Ni₅P₄ a superior catalytic activity.³⁴

WO₃ has a perovskite structure built by the corner- and edge-sharing octahedra, which allows multiple polymorphs, including monoclinic, triclinic, orthorhombic, tetragonal, hexagonal, and cubic phases, depending on the tilt angle and rotation direction of the octahedra.³⁵ Theoretical calculations have predicted that the presence of V_Os in WO₃ increases the symmetry of crystal phase and this would affect the electronic structure as well as its work function.³⁶ However, there is no experimental report to support this argument up to date. Previously, cubic phase WO_{3-x} nanostructures, which possess the highest symmetry in the WO₃ polymorph family, have been

prepared by annealing WO_3 at high temperatures ($\geq 500\text{ }^\circ\text{C}$) without cation intercalation.^{23, 37} Nonetheless, both studies only demonstrated the improved conductivity and optical absorptivity of cubic WO_{3-x} nanostructures compared with pristine WO_3 , without evaluating the photocatalytic properties or examining the band structure. Notably, the cubic phase WO_{3-x} prepared with this method were metastable only in a certain temperature range, and they were converted back to monoclinic phase upon cooling.³⁸

Herein, we demonstrate that a mild wet chemical method can regulate the V_{OS} , crystal phase, and electronic structure of WO_3 to effectively tune the photocatalytic HER activity. By modulating the ratio of reductant (trioctylphosphine, TOP) and reduction promoter (trioctylphosphine oxide, TOPO), the number of induced V_{OS} is varied to give WO_{3-x} nanoplates of different crystal structures that are stable under ambient conditions. Experimental and computational calculation results reveal the upshifts of both CBM and Fermi level (E_{F}) with respect to the pristine WO_3 in monoclinic phase ($m\text{-WO}_3$). The reformed band structure of WO_{3-x} allows the photocatalytic HER without the assistance of co-catalyst. A maximum steady H_2 generation rate of $340\text{ }\mu\text{mol g}^{-1}\text{ h}^{-1}$ is achieved under simulated sunlight, which is the highest HER rate for WO_3 and/or WO_{3-x} to the best of our knowledge. Our work demonstrates that treating WO_3 with mild reducing agents is a simple yet effective way to tailor the crystal structure and optical band structure via induced V_{OS} , which endows new catalytic functions.

Results and Discussion

Monoclinic WO_3 nanoplates ($m\text{-WO}_3$) were synthesized by the hydrothermal reaction of sodium tungstate and nitric acid at $180\text{ }^\circ\text{C}$.³⁹ The as-prepared $m\text{-WO}_3$ nanoplates were dispersed in oleylamine and stirred in the presence of a TOP–TOPO mixture (mole ratio of TOP:TOPO = 1:0,

2:1, 1:1, 1:2, and 0:1 with the amount of TOP fixed at 5 mL) at 320 °C under N₂ for 3 h to yield a distinct color change from pale yellow to a series of blue colors of different brightness (Figure 1a). Such color changes were previously reported to arise from either crystal phase modification^{23, 40} or surface V_{OS}.^{18, 26, 29} We first engaged the X-ray diffraction (XRD) analysis to investigate the crystal phase change induced by the TOP–TOPO treatment, and the results are summarized in Figure 1b. The XRD pattern of pristine *m*-WO₃ matches well with the reference card (JCPDS no. 43-1035). The sharp diffraction peaks indicate the crystalline nature, and the major peaks at 23.1°, 23.6°, 25.0°, 33.3°, and 34.3° are indexed to (002), (020), (200), (022), and (202) planes of monoclinic phase WO₃, respectively. The sample treated with only TOP (W-10) shows a slightly different pattern with the same sharpness, where the peaks observed at 28.8° and 59.7° can be ascribed to (111) and (222) planes of orthorhombic phase WO₃ (JCPDS no. 20-1324). From a control experiment in which the pristine *m*-WO₃ was heated in the absence of TOP (W-00), no change in the XRD pattern was observed, indicating that the transition to orthorhombic phase is induced by the TOP treatment. The cell symmetry of WO₃ is known to increase, from monoclinic to orthorhombic and/or cubic phase, by annealing under reducing environments, such as H₂ and NH₃.^{23, 37, 41} In our case, TOP, an effective reducing agent in non-polar solvents, is believed to reduce W⁶⁺ to a lower oxidation state (W⁵⁺ or W⁴⁺), thus triggering the phase transition.^{42, 43} It has been proposed that the increased electron density in the lattice of WO₃ would weaken the W–O bond and lead to the distortion of WO₆ octahedra, resulting in the phase transformation to a higher symmetry structure.^{44, 45}

The sample treated with a 2:1 mixture of TOP and TOPO (W-21) exhibits a similar diffraction pattern as W-10 but with broader peak widths, suggesting a reduced crystallinity due to the modified crystal structure or the coexistence of both monoclinic and orthorhombic phases. Further

increase of TOPO (TOP:TOPO = 1:1, W-11) leads to a prominent change of diffraction pattern. In particular, two sets of three peaks at *ca.* 23.6° and 33.6° merge to appear as two broad single peaks. The observed pattern is closely related to the cubic phase of WO₃ (JCPDS no. 46-1096) with slight shifts to lower angles, probably due to the lattice expansion caused by V_{Os}.²³ From the cell refinement, the lattice expansion was confirmed by the increased lattice constant *a* from 7.521 to 7.552 Å. Interestingly, the higher dose of TOPO (TOP:TOPO = 1:2, W-12) during the treatment reverts the XRD pattern to orthorhombic phase. Furthermore, when only TOPO was used in the synthesis (W-01), no phase transition occurred as revealed by its monoclinic XRD pattern. It is believed that both TOP and TOPO play important but different roles in the phase transition of WO₃. Through the lone pair electrons on the phosphine oxide moiety, TOPO can bind to the surface W sites.^{46, 47} This TOPO–W bonding can assist the loss of O to TOP and thus the reduction of W. By adjusting the ratio of TOP and TOPO, a reducing agent and promoter, the phase transition of WO₃ could be modulated. To gain a better insight on the process of phase transition, we conducted a time-resolved XRD analysis during the preparation of W-11 (Figure S1). The initial monoclinic WO₃ was shortly transformed to the orthorhombic phase after 30 min of heating. The broadening of peaks observed at 1 h reaction indicates the initiation of second transformation, which is completed as a cubic-like pattern after 3 h.

In conjunction with the phase transition of WO₃, a gradual color change from yellow to light and dark blue was observed (Figure 1a). We investigated the light responses of the samples using UV-Vis diffuse reflectance spectroscopy (UV-Vis DRS) and the spectra are given in Figure S2. From the significant absorption tails in the visible region (450–800 nm), it is evident that the light absorption of W-10 and W-11 have been extended. Such extended absorptions in the visible region may be related to the changes in particle size,⁴⁸ exposed crystal faces,⁴⁹ and/or defect sites.^{2, 26, 28}

We first measured Raman spectra to investigate the oxygen vacancies (V_{Os}) induced by TOP–TOPO treatment (Figure 1c). Both orthorhombic (W-10) and cubic-like (W-11) samples display two sets of characteristic Raman peaks for WO_3 , similar to $m-WO_3$. Two peaks at ca. 261 and 326 cm^{-1} are assigned to the $W^{6+}-O-W^{6+}$ bending vibration mode of bridging oxygen in WO_3 crystal lattice, whereas those observed at ca. 703 and 806 cm^{-1} are attributed to the long and short $W^{6+}-O-W^{6+}$ bond stretching mode, respectively.¹⁷ Compared to the pristine $m-WO_3$, both W-10 and W-11 display largely reduced peak intensities, suggesting the weakening of W–O bond due to the partial removal of oxygen atoms from the lattice.^{23, 50} In addition, most peaks, especially those at 261 and 703 cm^{-1} in $m-WO_3$ spectrum, are blue-shifted, which indicates the decrease in W–O bond strength. It is presumably due to the outward motion of the W after the removal of O from W–O–W bonding, which consequently compresses its bonding with other neighboring O atoms along the W– V_O –W direction. This agrees well with the first-principles studies previously reported.⁴⁴

The presence of V_{Os} in the TOP–TOPO treated samples was confirmed by electron paramagnetic resonance (EPR) studies, which is an effective technique to characterize the magnetic properties of nanomaterials. WO_3 is antimagnetic showing no EPR signal. The V_{Os} sites created on the WO_3 can trap the electrons to produce paramagnetic resonance with $S = 1/2$. Thus, a stable EPR signal with g -value of 2.002 is expected.^{51–53} From both W-10 and W-11, a distinct symmetric EPR signal is observed at the g -value of 2.002, indicating the presence of V_{Os} (Figure 1d).^{21, 54} A much intense signal from W-11 suggests more V_{Os} present.²⁴ In contrast, no peak is observed from $m-WO_3$. The EPR studies, jointly with Raman results, indicate that the TOP–TOPO treatment creates V_{Os} that can lead to phase transition, as supported by XRD results. To better represent their crystal phase and chemical composition, hereinafter, orthorhombic W-10 and pseudo-cubic W-11 are referred as $o-WO_{3-x}$ and $pc-WO_{3-x}$, respectively.

Figures 2a–c show transmission electron microscopic (TEM) images of as-prepared *m*-WO₃, *o*-WO_{3-x}, and *pc*-WO_{3-x} nanocrystals. All three samples display the rectangular nanoplate morphology with similar average sizes (*m*-WO₃ = 131 nm × 117 nm; *o*-WO_{3-x} = 139 nm × 122 nm; *pc*-WO_{3-x} = 130 nm × 112 nm). They also have a similar thickness of *ca.* 68 nm based on the scanning electron microscopic (SEM) images shown in Figure S3. Well-ordered lattice fringes are visible from the high resolution TEM (HR-TEM) images of all samples (Figures 2d–f), indicating their high crystallinity. The *d*-spacing values of those lattice fringes exhibit subtle but clear differences. The *d*-spacing of *m*-WO₃ lattice fringes is 0.384 nm which can be indexed to the (002) plane of monoclinic phase. The corresponding fast Fourier transform (FFT) pattern (inset in Figure 2d) confirms the single-crystal spots of the (002) plane. From *o*-WO_{3-x}, *d*-spacing of 0.390 nm is measured and indexed to (001) plane of orthorhombic phase, which is supported by the corresponding FFT pattern (inset in Figure 2e). The *d*-spacing of 0.376 nm observed from *pc*-WO_{3-x} can be correlated to (200) plane of cubic phase. It is noteworthy that *o*- and *pc*-WO_{3-x} retain the morphology, size, and crystallinity of *m*-WO₃, indicating that the TOP–TOPO treatment causes no major structural deformation.

We have employed X-ray photoelectron spectroscopy (XPS) to investigate the surface composition and charge state of atoms, and the results are presented in Figures 3 and S4. In the survey XPS spectra (Figure S4), only W and O signals are identified from all three samples, with a tiny C 1s peak due to the adsorbed carbon-containing species. The normalized W 4*f* core level spectra (Figure 3a) show distinct differences among the samples. The W 4*f* spectrum of *m*-WO₃ detects only W⁶⁺ ions with the peaks at binding energies of 35.0 and 37.1 eV which belong to W 4*f*_{5/2} and W 4*f*_{7/2}, respectively. Similar but broader peaks are found in the W 4*f* spectrum of *o*-WO_{3-x} at the slightly higher binding energies. Peak fitting reveals W⁵⁺ peaks at binding energies of 34.5 and

36.7 eV,²⁸ in addition to W⁶⁺ state at 35.5 and 37.7 eV. The W 4f spectrum of *pc*-WO_{3-x} shows the further shift and broadening of peaks, where W⁴⁺ ions are identified at binding energies of 33.4 and 35.8 eV^{23, 26} together with W⁶⁺ (35.7 and 37.9 eV) and W⁵⁺ states (34.5 and 36.7 eV). This is in good accordance with the EPR studies and further validates the reduction of W⁶⁺ to the lower oxidation states by TOP. The O 1s spectra of both *o*- and *pc*-WO_{3-x} exhibit a broad peak (Figure 3b), which can be deconvoluted into two peaks. The peaks centered at 530.4 eV (*o*-WO_{3-x}) and 530.5 eV (*pc*-WO_{3-x}) are ascribed to the lattice O²⁻ species (W–O–W),²¹ while the other peak at 531.8 eV in both *o*- and *pc*-WO_{3-x} is assigned to O²⁻ in the vicinity of V_{Os} (W–O–H).⁵⁰ Meanwhile, the O 1s spectrum of *m*-WO₃ shows a major peak for lattice oxygen atoms at 529.9 eV with a small peak at 531.8 eV presumably due to the surface contamination during sample preparation.

Both W 4f and O 1s peaks are notably shifted to the higher binding energies by ca. 0.6 and 0.5 eV in *o*-WO_{3-x} and ca. 0.8 and 0.6 eV in *pc*-WO_{3-x}, respectively, compared to those of *m*-WO₃. The shift of W⁶⁺ peak is attributed to the change in the electron chemical potential of *o*- and *pc*-WO_{3-x} as a result of the change in local atomic structure, *i.e.*, crystal phase.^{55, 56} The electron chemical potential represents the Fermi energy (E_F) relative to the absolute vacuum level (E_{V∞}), thus, such increments suggest the upshift of E_F towards E_{V∞}. On the other hand, the formation of V_{Os} leads to the increased binding energy of remaining O around W and hence shifts O 1s peak to a higher binding energy.^{57, 58} As this shift of O 1s peak is dependent on the V_{Os} concentration,⁵⁵ the greater shift in *pc*-WO_{3-x} spectrum implies the higher concentration of V_{Os}. Also, the intensity of peak at 531.8 eV (assigned to O²⁻ in the vicinity of V_{Os}) is higher in *pc*-WO_{3-x} spectrum, supporting that more V_{Os} are created in *pc*-WO_{3-x}. The elemental ratio calculated by XPS analysis confirms this by the lowest surface O to W ratio in *pc*-WO_{3-x} (Table S1; 3, 2.76, and 2.69 for *m*-WO₃, *o*-WO_{3-x},

and $pc\text{-WO}_{3-x}$, respectively), which is in good agreements with the EPR results that show the highest V_O concentration in $pc\text{-WO}_{3-x}$.

The V_{OS} and crystal phase have profound effects on the electronic structure and may alter the physicochemical properties of nanomaterials.^{2, 59-62} Intrigued by the fact that a simple TOP–TOPO treatment can induce V_{OS} on $m\text{-WO}_3$ and adjust its crystal phase, we further investigated the changes in the electronic structure. By fitting the UV-Vis DRS spectra to the Tauc equation, the band gap energies (E_g) of the samples are calculated to be 2.70, 2.65, and 2.62 eV for $m\text{-WO}_3$, $o\text{-WO}_{3-x}$, and $pc\text{-WO}_{3-x}$, respectively (Figure S2). Despite the obvious color change, rather similar E_g values were measured. The valence band XPS (VB-XPS) spectra, however, reveal the changes in the electron band structure and band offset (Figure 4a). The position of VB maximum (VBM) was first evaluated by linearly extrapolating the onset of VB-XPS spectra to the baseline, which reflects a band edge position with respect to the E_F . The VBM edge levels of $m\text{-WO}_3$, $o\text{-WO}_{3-x}$, and $pc\text{-WO}_{3-x}$ were determined to be 2.65, 2.48, and 2.32 eV, respectively, indicating the upshift of VBM by the induced V_{OS} . By constructing the Mott-Schottky plots, we have determined the E_F to obtain the band structure.^{29, 63, 64} Figure 4b compares the flat band potentials, which reflects the difference between the E_F level and the water reduction potential of the samples. From $m\text{-WO}_3$ to $o\text{-WO}_{3-x}$ and $pc\text{-WO}_{3-x}$, the flat band potential shifts from 0.1 to 0 and -0.15 V, which verifies the reconstruction of electronic structure in consistence with the peak shifts observed in the XPS studies.

Based on the results from UV-Vis DRS, VB-XPS, and Mott–Schottky plots, we have constructed the energy level diagrams that qualitatively represent the changes in band structure of $o\text{-}$ and $pc\text{-WO}_{3-x}$ (Figure 4c). The conduction band minimum (CBM) was estimated according to the equation of $E_{CBM} = E_{VBM} - E_g$. From the Mott-Schottky plot ($E_F = 0.1$ V) and VB-XPS (flat band

potential = 2.65 eV), the E_{VBM} of $m\text{-WO}_3$ was calculated to be 2.75 eV and the observed E_g of 2.70 eV yields the E_{CBM} of 0.05 eV.^{65, 66} The upshift of E_F , apparently due to the induced V_{Os} and phase transition, pushes up the E_{VBM} from 2.75 to 2.48 eV for $o\text{-WO}_{3-x}$, and to 2.17 eV for $pc\text{-WO}_{3-x}$. The E_{CBM} are determined to be -0.17 and -0.45 eV for $o\text{-WO}_{3-x}$ and $pc\text{-WO}_{3-x}$, respectively, which satisfies the thermodynamic requirement for the reduction of water to H_2 .

To verify the reconstruction of band structures in $o\text{-}$ and $pc\text{-WO}_{3-x}$, we have carried out the photocatalytic HER using a mixed solution of Na_2S (0.35 M) and Na_2SO_3 (0.25 M) as a sacrificial agent under one sun illumination. Both $o\text{-}$ and $pc\text{-WO}_{3-x}$ show photocatalytic HER activities with the average H_2 generation rates of 268 and 340 $\mu\text{mol g}^{-1} \text{h}^{-1}$, respectively. The control experiments conducted under the dark and using $m\text{-WO}_3$ as photocatalyst generated no detectable H_2 . To the best of our knowledge, this is the best performance for photocatalytic HER from WO_3 without any co-catalysts. The H_2 generation rate by $pc\text{-WO}_{3-x}$ is stable during the continuous 24 h reaction, showing no discernable degradation in the catalytic activity (Figure 5a). The TEM analyses of the samples after the photocatalysis reveal that the nanoplates still retain the rectangular morphologies with a few rounded corners (Figures 5b and S5). The post-catalysis HR-TEM images confirm the retention of crystallinity by unchanged and well-ordered lattice fringes.

First-principles calculations based on density functional theory (DFT) were also performed to better understand the role of V_{Os} in determining the structural and electronic properties of WO_3 . Removing a neutral O atom leaves two excess electrons. In bulk WO_3 , as shown in Figures 6a–c and S6, our hybrid DFT calculations predict the excess electrons to be largely delocalized by filling the bottom of the conduction band, rather than creating localized states in the bandgap, especially when the V_{O} concentration is relatively low such that V_{Os} are well separated from each other. The V_{O} formation energy is predicted to decrease as the vacancies undergo aggregation along the W–

O–W chain, which is mainly attributed to the itinerant nature of the excess charge. The shallow-donor nature of V_{OS} in WO_3 has also been predicted by previous hybrid DFT studies.⁴⁴ However, when V_{OS} cluster together to form an extended state, our calculations also show the creation of a well-localized state close to the conduction band, implying that the excess electrons are not fully itinerant (see supporting information). In general, the shallow behavior of V_{OS} could explain why the resistivity of WO_3 decreases with increasing V_{OS} ;⁶⁷ the increase in electrical conductivity may also contribute to improving the separation efficiency of photogenerated electron-hole pairs. In contrast to the case of bulk, the excess electrons generated due to surface and subsurface V_{OS} are found to be mainly localized on the W atoms adjacent to each vacancy, creating in-gap states as demonstrated in Figure S7. This suggests that the reduction of W^{6+} to a lower oxidation state (W^{5+} or W^{4+}) as observed by XPS may originate from the creation of V_{OS} .

As pointed out earlier, stoichiometric WO_3 exhibits a monoclinic crystalline structure under typical reaction conditions. According to our hybrid (standard) DFT calculations, the cubic phase is predicted to be about 0.14 (0.09) eV per formula unit less thermodynamically favorable compared to the monoclinic phase, while there is no significant difference in stability between the monoclinic and orthorhombic phases. As summarized in Table S2, the relative stabilities of the different phases are likely to be strongly affected by the presence of V_{OS} . As the V_O concentration increases, the energy difference between the monoclinic and cubic phases tends to monotonically decrease, and it becomes only 0.06 (0.04) eV per formula unit at $x = 0.375$ in WO_{3-x} . This implies that the cubic-like structural features can be observed when the V_O concentration is sufficiently high. In addition, when $x > 0.1$ in WO_{3-x} , our calculations predict that the monoclinic and orthorhombic phases have very similar thermodynamic stabilities, suggesting a possible transition between these

two phases. Our calculation results are overall consistent with the experimentally observed change from low-symmetry to high-symmetry structures.

For stoichiometric WO_3 , as shown in Figures 6a–c and S6, the CBM is composed of W $5d$ states with some hybridization with O $2p$ states while the VBM is primarily composed of nonbonding O $2p$ states. The W $5d$ –O $2p$ hybridized states are sensitive to variations in the W–O–W tilt angle between adjacent WO_6 octahedra. With increasing the W–O–W tilt angle from the monoclinic to cubic phases, the CBM is substantially downshifted, thereby leading to a monotonic decrease in the band gap.⁶⁸ The VBM of the cubic and orthorhombic phases are predicted to be comparable while somewhat higher in energy than the monoclinic phase.⁶⁹ Upon creation of V_{Os} , the excess electrons fill the W $5d$ –O $2p$ hybridized states; the partially filled hybrid states are found to be upshifted. The energy difference between the partially filled W $5d$ –O $2p$ hybrid and nonbonding O $2p$ states becomes larger with increasing V_{Os} ; when the V_{Os} concentration is sufficiently large, the energy difference even in the cubic phase tends to be comparable to the bandgap of the monoclinic phase. This analysis suggests that both CBM and VBM could be substantially upshifted with no significant reduction in the band gap by the presence of V_{Os} , consistent with the characterization results described earlier.

Finally, we evaluated the hydrogen binding on $\text{WO}_3(001)$ surface as shown in Figure 6d. Our calculations show that H atom is preferably bound to a protruding surface O atom. The hydrogen binding energy is predicted to be $E_{\text{b}}(\text{H}) = 0.38$ eV by DFT-GGA (PBE) calculations with the $2 \times 2 \times 9$ slab model in Figures 6d–e; here, $E_{\text{b}}(\text{H})$ is given by $(E_{\text{slab}} + E_{\text{H}_2} - E_{2\text{H}/\text{slab}})/2$, where E_{slab} , E_{H_2} , and $E_{2\text{H}/\text{slab}}$ are the energies of the slab, gaseous H_2 , and the slab with two H atoms on the top and bottom surfaces, respectively. As demonstrated in Figure 6e, excess electrons tend to largely localize on protruding surface O atoms; when two excess electrons are added to the slab, the

predicted $E_b(H)$ substantially decreases to 0.16 eV. This implies that the enhanced HER activity could be also related to the excess charge resulting from V_{OS} creation, given the performance of a HER catalyst primarily relies on the hydrogen binding strength.

Conclusions

In conclusion, we demonstrated that the crystal phase of WO_3 can be regulated by a simple and mild TOP–TOPO treatment. The induced V_{OS} in m - WO_3 , depending on the amount, leads to a distortion of WO_6 octahedra, resulting in the formation of reduced orthorhombic and pseudo-cubic WO_{3-x} . Such changes exert a significant effect on the electron chemical potential of the samples, thus shifting the CBM above the H_2 reduction potentials, as supported by our DFT calculations. The pc - WO_{3-x} , which can host the highest amount of V_{OS} , affords the highest photocatalytic H_2 production rate of $340 \mu\text{mol g}^{-1} \text{h}^{-1}$ without any co-catalysts. This work is the first example of controlling the crystal phases of WO_3 with introduced V_{OS} to effectively tune the band structure and extend its catalytic application to H_2 generation from water.

Experimental Section

Materials. Sodium tungstate ($Na_2WO_4 \cdot 2H_2O$, 98%), nitric acid (HNO_3 , 68%), trioctylphosphine (TOP, 97%), trioctylphosphine oxide (TOPO, 98%), and oleylamine (OLA, 80-90%) were purchased from Sigma-Aldrich. All chemicals were used as received.

Synthesis of monoclinic WO_3 nanocrystals (m - WO_3). Rectangular monoclinic WO_3 (m - WO_3) nanocrystals were synthesized according to the reported method³⁹ with slight modifications. In a typical synthesis, $Na_2WO_4 \cdot 2H_2O$ (1 mmol) was dissolved in deionized water (13 mL), to which HNO_3 (68 wt%, 12 mL) was added dropwise to form H_2WO_4 . The resulting solution was

transferred to a 50 mL Teflon-lined stainless-steel autoclave, sealed, and heated to 180 °C for 12 h. After cooled to room temperature, the precipitate was collected and washed with absolute ethanol and distilled water for three times, and dried at 60 °C.

Synthesis of orthorhombic (*o*-WO_{3-x}) and pseudo-cubic (*pc*-WO_{3-x}) WO_{3-x} nanocrystals. For the preparation of *o*-WO_{3-x} nanocrystals, as-synthesized *m*-WO₃ (0.2 g) was first transferred to a three-necked round bottom flask containing 5 mL of oleylamine and gently stirred under vacuum for 10 min to remove adventitious oxygen and moisture. To this solution, TOP (5 mL) was injected and the mixture was heated to 320 °C under N₂ for 3 h. After cooling the solution to 80 °C, the product was collected and washed by repeated solution/desolution processes with ethanol and chloroform. The final product was dried at room temperature and stored under vacuum for further use. For *pc*-WO_{3-x} nanocrystals, the same procedure was adapted except for the extra addition of TOPO (4.3 g, mole ratio of TOP:TOPO = 1:1) before heating.

Material characterizations. Powder X-ray diffraction (XRD) patterns were obtained using a Rigaku SmartLab X-ray diffractometer with Cu K α radiation of 1.5406 Å. The spectra were collected at 2 θ from 20° to 70° with a step size of 0.2° at a rate of 10° min⁻¹. Transmission electron microscopic (TEM) images were taken using a JEOL JEM-2100F STEM operated at 200 kV. Samples for TEM analysis were prepared by drop-casting the nanocrystals dispersed in chloroform onto a holey carbon-coated 400 mesh Cu TEM grid. The elemental compositions were determined by an energy dispersive spectrometer (EDS) equipped in the STEM. UV-Vis diffuse reflectance spectra were taken by Cary 4000 UV-Vis Spectrophotometer. Raman spectroscopic measurements were performed on a Raman spectrometer (Renishaw, InVia Raman microscope) with an excitation wavelength of 786 nm. X-ray photoelectron spectroscopy (XPS) were conducted using

an X-ray Photoelectron spectrometer (ESCALAB 250Xi, Thermo Fisher) with a monochromic Al K α X-ray source and a pass energy of 1,486.6 eV.

Electrochemical measurements. Mott-Schottky plot was constructed based on the electrochemical measurements using a typical three electrode system where Ag/AgCl (in 3 M NaCl solution) and graphite were used as the reference and counter electrodes in a phosphate buffer (pH = 7.4). The as-synthesized *m*-WO₃, *o*-WO_{3-x}, and *pc*-WO_{3-x} were deposited onto a glassy carbon electrode (GCE) and used as a working electrode. The required data were collected via measuring the space charge layer capacitance over a scanned range of applied potentials (−1.0 to 0.5 V) at 1,000 Hz using a CHI 700E electrochemical station. The recorded potentials were referenced to a reversible hydrogen electrode (RHE) according to the following equation:

$$E \text{ (V vs. RHE)} = E \text{ (V vs. Ag/AgCl)} + 0.197 + 0.0592 \times \text{pH}$$

Photocatalytic HER. Catalyst (3 mg) was dispersed in an aqueous solution (25 mL) containing the sacrificial agent, a mixture of 0.35 M Na₂S and 0.25 M Na₂SO₃. After degassing with argon for 30 min, the suspended solution was then irradiated with a solar simulator (Newport, ozone free 150 W Xe lamp) equipped with an AM 1.5 air-mass filter. The reaction product in the headspace was periodically sampled with a gas-tight syringe and analyzed by an Agilent 7890 B gas chromatograph equipped with a thermal conductivity detector (TCD) using nitrogen as carrier gas.

First-principles calculations. We employed the Heyd-Scuseria-Ernzerhof (HSE06) hybrid functional^{70, 71} and the Perdew-Burke-Ernzerh (PBE)⁷² generalized gradient approximation (GGA) with and without Hubbard U corrections,⁷³ as implemented in the Vienna ab initio simulation package.⁷⁴ We employed the projector augmented wave method and a planewave basis set. All atoms in bulk supercells were fully relaxed until the residual forces were less than 0.01 eV/Å. For the 2×2×9 slab, the middle three atomic layers were fixed in their bulk positions and all other

atoms were fully relaxed, with a vacuum space of 30 Å to minimize interactions between periodic images. Periodic boundary conditions were applied in all three dimensions.

Figures

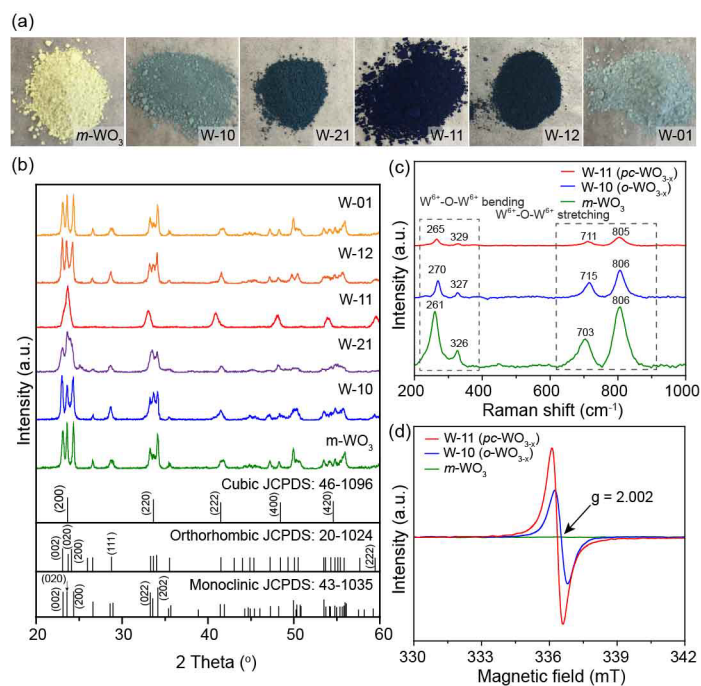


Figure 1. (a) Photographs of pristine and TOP/TOPO-treated WO_3 samples. The numbers in sample name denote the TOP:TOPO ratio. (b) The corresponding XRD spectra of pristine and TOP/TOPO-treated WO_3 samples. (c) Raman and (d) EPR spectra of $m\text{-WO}_3$, W-10 ($o\text{-WO}_{3-x}$), and W-11 ($pc\text{-WO}_{3-x}$).

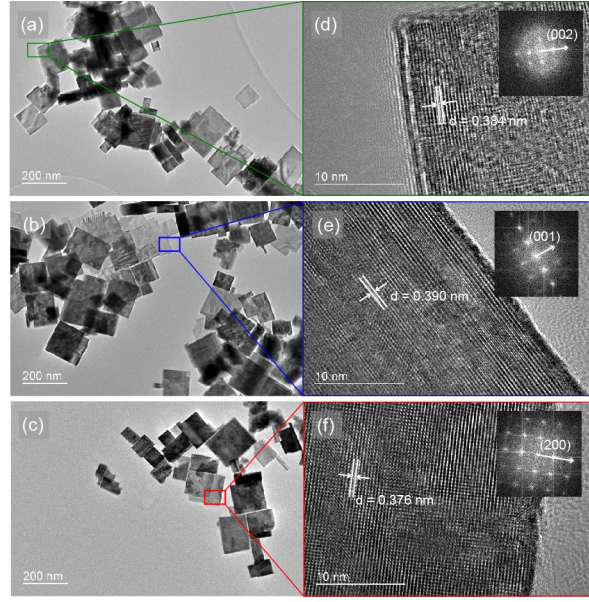


Figure 2. TEM images of (a, d) m - WO_3 , (c, b) o - WO_{3-x} , and (e, f) pc - WO_{3-x} . Insets in (d), (e), and (f) show the FFT patterns of the selected areas.

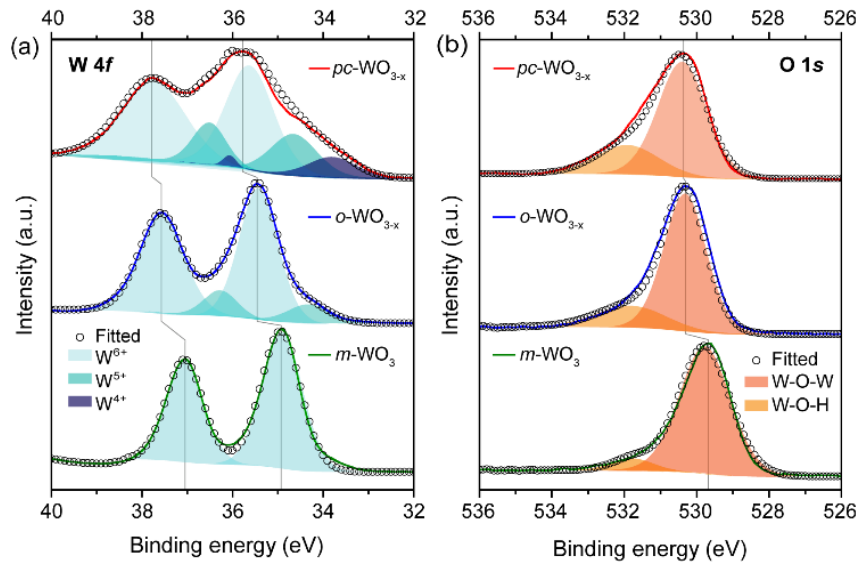


Figure 3. (a) W 4f and (b) O 1s XPS spectra of m - WO_3 (bottom), o - WO_{3-x} (middle), and pc - WO_{3-x} (top).

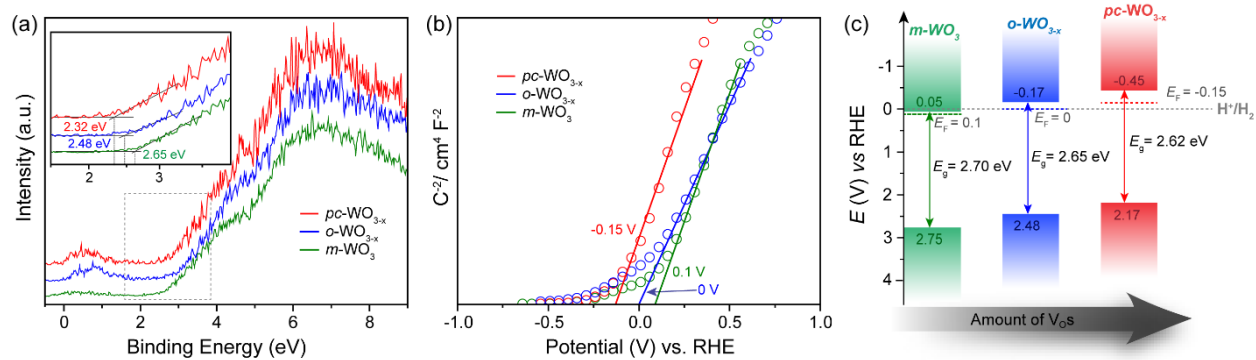


Figure 4. (a) VB-XPS spectra and (b) Mott-Schottky plots of $m-WO_3$, $o-WO_{3-x}$, and $pc-WO_{3-x}$. Inset in (a) is the enlarged area near the band edges indicated by a dotted box. (c) Schematic illustration of the energy levels of $m-WO_3$, $o-WO_{3-x}$, and $pc-WO_{3-x}$.

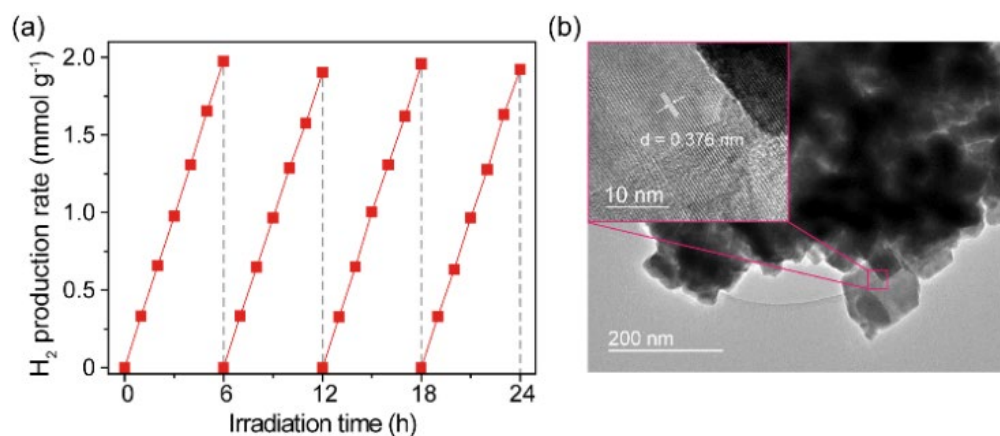


Figure 5. (a) Photocatalytic H_2 production using $pc-WO_{3-x}$ as a photocatalyst for 24 h reaction of four cycles. (b) Low-resolution TEM image of $pc-WO_{3-x}$ after photocatalysis. Inset in (b) is the high-resolution TEM image of the selected area.

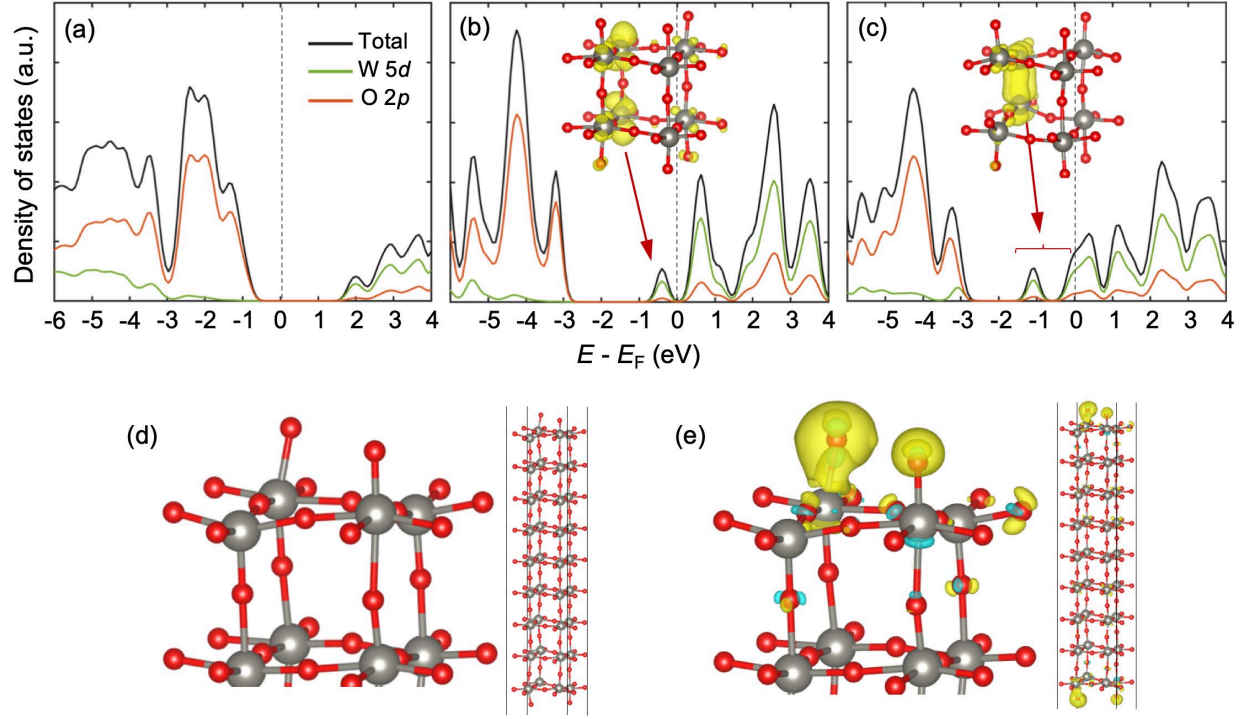


Figure 6. *Top panel:* Electron density of states (DOS) of $m\text{-WO}_{3-x}$ with different concentrations of oxygen vacancies in a 32-atom supercell; (a) $x = 0$, (b) $x = 0.125$, and (c) $x = 0.375$, from hybrid DFT calculations with $E_{\text{cut}} = 600$ eV and Γ -centered $(4 \times 4 \times 4)$ Monkhorst-Pack k-point mesh. The energy zero is set at the Fermi level (E_F) which is indicated by the vertical dashed line. The insertions show band-decomposed charge density of the partially filled W 5d-O 2p hybridized states (with an isosurface value of $0.005 \text{ e } \text{\AA}^{-1}$). *Bottom panel:* WO_3 surface structures created using a $2 \times 2 \times 9$ slab with (d) no excess electron and (e) two excess electrons, from DFT-GGA (PBE) calculations with $E_{\text{cut}} = 500$ eV and Γ -centered $(2 \times 2 \times 1)$ k-point mesh. The charge density difference plot in (e) clearly demonstrates that excess electrons are mostly localized on the protruding surface oxygen atoms; Blue and yellow isosurfaces (at $0.0015 \text{ e } \text{\AA}^{-1}$) indicate electron loss and electron gain, respectively. Grey and red balls represent W and O atoms, respectively.

ASSOCIATED CONTENT

Supporting Information. The supporting information is available free of charge on the ACS Publication website at <http://pubs.acs.org>.

AUTHOR INFORMATION

Corresponding Authors

* Email: gshwang@che.utexas.edu (G. S. Hwang), lawrence.ys.lee@polyu.edu.hk (L. Y. S. Lee)

Notes

The authors declare no competing financial interest.

ACKNOWLEDGMENT

This work was supported by the Innovation and Technology Commission of Hong Kong and the Hong Kong Polytechnic University (Grant No. 1-BE0Y). G.S.H. gratefully acknowledges the support from the R.A. Welch Foundation (No. F-1535). We also acknowledge the technical support from the University Facility in Life Science (ULS) of the Hong Kong Polytechnic University and thank the Texas Advanced Computing Center for use of the Stampede supercomputing system (OCI-1134872).

References

- (1) Concina, I.; Ibupoto, Z. H.; Vomiero, A., Semiconducting Metal Oxide Nanostructures for Water Splitting and Photovoltaics. *Adv. Energy Mater.* **2017**, 7, 1700706.
- (2) Huang, Z.-F.; Song, J.; Pan, L.; Zhang, X.; Wang, L.; Zou, J.-J., Tungsten Oxides for Photocatalysis, Electrochemistry, and Phototherapy. *Adv. Mater.* **2015**, 27, 5309-5327.
- (3) Bignozzi, C. A.; Caramori, S.; Cristino, V.; Argazzi, R.; Meda, L.; Tacca, A., Nanostructured photoelectrodes based on WO₃: applications to photooxidation of aqueous electrolytes. *Chem. Soc. Rev.* **2013**, 42, 2228-2246.
- (4) Khoomortezaei, S.; Abdizadeh, H.; Golobostanfard, M. R., Triple Layer Heterojunction WO₃/BiVO₄/BiFeO₃ Porous Photoanode for Efficient Photoelectrochemical Water Splitting. *ACS Appl. Energy Mater.* **2019**, 2, 6428-6439.
- (5) Zhang, J.; Liu, Z.; Liu, Z., Novel WO₃/Sb₂S₃ Heterojunction Photocatalyst Based on WO₃ of Different Morphologies for Enhanced Efficiency in Photoelectrochemical Water Splitting. *ACS Appl. Mater. Interfaces* **2016**, 8, 9684-9691.
- (6) Zhang, L. J.; Li, S.; Liu, B. K.; Wang, D. J.; Xie, T. F., Highly Efficient CdS/WO₃ Photocatalysts: Z-Scheme Photocatalytic Mechanism for Their Enhanced Photocatalytic H₂ Evolution under Visible Light. *ACS Catal.* **2014**, 4, 3724-3729.
- (7) Sivula, K.; Formal, F. L.; Grätzel, M., WO₃-Fe₂O₃ Photoanodes for Water Splitting: A Host Scaffold, Guest Absorber Approach. *Chem. Mater.* **2009**, 21, 2862-2867.
- (8) Liu, C.; Huang, H.; Cui, W.; Dong, F.; Zhang, Y., Band structure engineering and efficient charge transport in oxygen substituted g-C₃N₄ for superior photocatalytic hydrogen evolution. *Appl. Catal. B Environ.* **2018**, 230, 115-124.
- (9) Mitra, A.; Howli, P.; Sen, D.; Das, B.; Chattopadhyay, K. K., Cu₂O/g-C₃N₄ nanocomposites: an insight into the band structure tuning and catalytic efficiencies. *Nanoscale* **2016**, 8, 19099-19109.
- (10) Schlesinger, R.; Bianchi, F.; Blumstengel, S.; Christodoulou, C.; Ovsyannikov, R.; Kobin, B.; Moudgil, K.; Barlow, S.; Hecht, S.; Marder, S. R.; Henneberger, F.; Koch, N., Efficient light emission from inorganic and organic semiconductor hybrid structures by energy-level tuning. *Nat. Commun.* **2015**, 6, 6754.
- (11) Chen, X.; Liu, L.; Yu, P. Y.; Mao, S. S., Increasing Solar Absorption for Photocatalysis with Black Hydrogenated Titanium Dioxide Nanocrystals. *Science* **2011**, 331, 746-750.
- (12) Wang, J.; Wang, Z.; Huang, B.; Ma, Y.; Liu, Y.; Qin, X.; Zhang, X.; Dai, Y., Oxygen Vacancy Induced Band-Gap Narrowing and Enhanced Visible Light Photocatalytic Activity of ZnO. *ACS Appl. Mater. Interfaces* **2012**, 4, 4024-4030.
- (13) Duan, H.; Dong, Y. Z.; Huang, Y.; Hu, Y. H.; Chen, X. S., The important role of oxygen vacancies in Sr₂MgSi₂O₇ phosphor. *Phys. Lett. A* **2016**, 380, 1056-1062.
- (14) Zhou, Z.; Liu, J.; Long, R.; Li, L.; Guo, L.; Prezhd, O. V., Control of Charge Carriers Trapping and Relaxation in Hematite by Oxygen Vacancy Charge: Ab Initio Non-adiabatic Molecular Dynamics. *J. Am. Chem. Soc.* **2017**, 139, 6707-6717.
- (15) Yang, Y.; Wang, Y.; Yin, S., Oxygen vacancies confined in SnO₂ nanoparticles for desirable electronic structure and enhanced visible light photocatalytic activity. *Appl. Surf. Sci.* **2017**, 420, 399-406.
- (16) Wang, C.; Wu, D.; Wang, P.; Ao, Y.; Hou, J.; Qian, J., Effect of oxygen vacancy on enhanced photocatalytic activity of reduced ZnO nanorod arrays. *Appl. Surf. Sci.* **2015**, 325, 112-116.

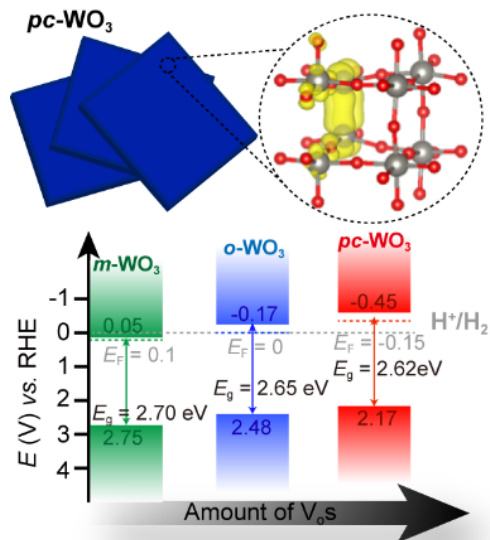
- (17) Bai, S.; Zhang, K.; Wang, L.; Sun, J.; Luo, R.; Li, D.; Chen, A., Synthesis mechanism and gas-sensing application of nanosheet-assembled tungsten oxide microspheres. *J. Mater. Chem. A* **2014**, *2*, 7927-7934.
- (18) Wang, G.; Ling, Y.; Wang, H.; Yang, X.; Wang, C.; Zhang, J. Z.; Li, Y., Hydrogen-treated WO₃ nanoflakes show enhanced photostability. *Energy Environ. Sci.* **2012**, *5*, 6180.
- (19) Liu, Q.; Wang, F.; Lin, H.; Xie, Y.; Tong, N.; Lin, J.; Zhang, X.; Zhang, Z.; Wang, X., Surface oxygen vacancy and defect engineering of WO₃ for improved visible light photocatalytic performance. *Catal. Sci. Technol.* **2018**, *8*, 4399-4406.
- (20) Li, W. D., P.; Zhang, Y.; Wang, Y.; Lin, X.; Gong, X.; Zheng, G., WO₃ Nanoflakes for Enhanced Photoelectrochemical Conversion. *ACS Nano* **2014**, *8*, 11700-11777.
- (21) Meng, J.; Lin, Q.; Chen, T.; Wei, X.; Li, J.; Zhang, Z., Oxygen vacancy regulation on tungsten oxides with specific exposed facets for enhanced visible-light-driven photocatalytic oxidation. *Nanoscale* **2018**, *10*, 2908-2915.
- (22) Li, Y.; Tang, Z.; Zhang, J.; Zhang, Z., Enhanced photocatalytic performance of tungsten oxide through tuning exposed facets and introducing oxygen vacancies. *J. Alloys Compd.* **2017**, *708*, 358-366.
- (23) Fang, Z.; Jiao, S.; Wang, B.; Yin, W.; Liu, S.; Gao, R.; Liu, Z.; Pang, G.; Feng, S., Synthesis of reduced cubic phase WO_{3-x} nanosheet by direct reduction of H₂WO₄ · H₂O. *Mater. Today Energy* **2017**, *6*, 146-153.
- (24) Zheng, T.; Sang, W.; He, Z.; Wei, Q.; Chen, B.; Li, H.; Cao, C.; Huang, R.; Yan, X.; Pan, B.; Zhou, S.; Zeng, J., Conductive Tungsten Oxide Nanosheets for Highly Efficient Hydrogen Evolution. *Nano Lett.* **2017**, *17*, 7968-7973.
- (25) Lv, Y.; Chen, Z.; Liu, Y.; Wang, T.; Ming, Z., Oxygen vacancy improves the hydrogen evolution reaction property of WO_{3-x} nanosheets. *Nano Struct. Nano Objects* **2018**, *15*, 114-118.
- (26) Song, J.; Huang, Z.-F.; Pan, L.; Zou, J.-J.; Zhang, X.; Wang, L., Oxygen-Deficient Tungsten Oxide as Versatile and Efficient Hydrogenation Catalyst. *ACS Catal.* **2015**, *5*, 6594-6599.
- (27) Yan, J.; Wang, T.; Wu, G.; Dai, W.; Guan, N.; Li, L.; Gong, J., Tungsten Oxide Single Crystal Nanosheets for Enhanced Multichannel Solar Light Harvesting. *Adv. Mater.* **2015**, *27*, 1580-1586.
- (28) Xi, G.; Ouyang, S.; Li, P.; Ye, J.; Ma, Q.; Su, N.; Bai, H.; Wang, C., Ultrathin W₁₈O₄₉ nanowires with diameters below 1 nm: synthesis, near-infrared absorption, photoluminescence, and photochemical reduction of carbon dioxide. *Angew. Chem. Int. Ed.* **2012**, *51*, 2395-9.
- (29) Wang, L.; Tsang, C.-S.; Liu, W.; Zhang, X.; Zhang, K.; Ha, E.; Kwok, W.-M.; Park, J. H.; Suk Lee, L. Y.; Wong, K.-Y., Disordered layers on WO₃ nanoparticles enable photochemical generation of hydrogen from water. *J. Mater. Chem. A* **2019**, *7*, 221-227.
- (30) Zhao, W.; Pan, J.; Fang, Y.; Che, X.; Wang, D.; Bu, K.; Huang, F., Metastable MoS₂: Crystal Structure, Electronic Band Structure, Synthetic Approach and Intriguing Physical Properties. *Chem. Eur. J.* **2018**, *24*, 15942-15954.
- (31) Zhang, J.; Xu, Q.; Feng, Z.; Li, M.; Li, C., Importance of the Relationship between Surface Phases and Photocatalytic Activity of TiO₂. *Angew. Chem. Int. Ed.* **2008**, *47*, 1766-1769.
- (32) Lukowski, M. A.; Daniel, A. S.; Meng, F.; Forticaux, A.; Li, L.; Jin, S., Enhanced Hydrogen Evolution Catalysis from Chemically Exfoliated Metallic MoS₂ Nanosheets. *J. Am. Chem. Soc.* **2013**, *135*, 10274-10277.

- (33) Su, R.; Bechstein, R.; Sør, L.; Vang, R. T.; Sillassen, M.; Esbjörnsson, B.; Palmqvist, A.; Besenbacher, F., How the Anatase-to-Rutile Ratio Influences the Photoreactivity of TiO₂. *J. Phys. Chem. C* **2011**, *115*, 24287-24292.
- (34) Pan, Y.; Liu, Y.; Zhao, J.; Yang, K.; Liang, J.; Liu, D.; Hu, W.; Liu, D.; Liu, Y.; Liu, C., Monodispersed nickel phosphide nanocrystals with different phases: synthesis, characterization and electrocatalytic properties for hydrogen evolution. *J. Mater. Chem. A* **2015**, *3*, 1656-1665.
- (35) Roussel, P.; Labbe, P. G., D., Symmetry and twins in the monophosphate tungsten bronze series (PO₂)₄(WO₃)_{2m} (2<=m<=14). *Acta Crystallogr. Sect. B: Struct. Sci.* **2000**, *56*, 377-391.
- (36) Walkingshaw, A. D.; Spaldin, N. A.; Artacho, E., Density-functional study of charge doping in WO₃. *Phys. Rev. B* **2004**, *70*, 165110.
- (37) Zhou, J.; Ding, Y.; Deng, S. Z.; Gong, L.; Xu, N. S.; Wang, Z. L., Three-Dimensional Tungsten Oxide Nanowire Networks. *Adv. Mater.* **2005**, *17*, 2107-2110.
- (38) Thummavichai, K.; Wang, N.; Xu, F.; Rance, G.; Xia, Y.; Zhu, Y., *In situ* investigations of the phase change behaviour of tungsten oxide nanostructures. *Royal Soc. Open Sci.* **2018**, *5*, 171932.
- (39) Zhang, H.; Liu, Z.; Yang, J.; Guo, W.; Zhu, L.; Zheng, W., Temperature and acidity effects on WO₃ nanostructures and gas-sensing properties of WO₃ nanoplates. *Mater. Res. Bull.* **2014**, *57*, 260-267.
- (40) Songara, S.; Gupta, V.; Kumar Patra, M.; Singh, J.; Saini, L.; Siddaramana Gowd, G.; Raj Vadera, S.; Kumar, N., Tuning of crystal phase structure in hydrated WO₃ nanoparticles under wet chemical conditions and studies on their photochromic properties. *J. Phys. Chem. Solids* **2012**, *73*, 851-857.
- (41) Chang, M.-T.; Chou, L.-J.; Chueh, Y.-L.; Lee, Y.-C.; Hsieh, C.-H.; Chen, C.-D.; Lan, Y.-W.; Chen, L.-J., Nitrogen-Doped Tungsten Oxide Nanowires: Low-Temperature Synthesis on Si, and Electrical, Optical, and Field-Emission Properties. *Small* **2007**, *3*, 658-664.
- (42) Liu, J.; Jeong, H.; Liu, J.; Lee, K.; Park, J. Y.; Ahn, Y. H.; Lee, S., Reduction of functionalized graphite oxides by trioctylphosphine in non-polar organic solvents. *Carbon* **2010**, *48*, 2282-2289.
- (43) Nancy, O.; E., S. S., Manipulating Local Ligand Environments for the Controlled Nucleation of Metal Nanoparticles and their Assembly into Nanodendrites. *Angew. Chem. Int. Ed.* **2012**, *51*, 11757-11761.
- (44) Wang, W.; Janotti, A.; Van de Walle, C. G., Role of oxygen vacancies in crystalline WO₃. *J. Mater. Chem. C* **2016**, *4*, 6641-6648.
- (45) Wang, F.; Di Valentin, C.; Pacchioni, G., Doping of WO₃ for Photocatalytic Water Splitting: Hints from Density Functional Theory. *J. Phys. Chem. C* **2012**, *116*, 8901-8909.
- (46) Becerra, L. R.; Murray, C. B.; Griffin, R. G.; Bawendi, M. G., Investigation of the surface morphology of capped CdSe nanocrystallites by ³¹P nuclear magnetic resonance. *J. Chem. Phys.* **1994**, *100*, 3297-3300.
- (47) Lorenz, J. K.; Ellis, A. B., Surfactant-Semiconductor Interfaces: Perturbation of the Photoluminescence of Bulk Cadmium Selenide by Adsorption of Tri-n-octylphosphine Oxide as a Probe of Solution Aggregation with Relevance to Nanocrystal Stabilization. *J. Am. Chem. Soc.* **1998**, *120*, 10970-10975.
- (48) Huang, J.-Y.; Madasu, M.; Huang, M. H., Modified Semiconductor Band Diagrams Constructed from Optical Characterization of Size-Tunable Cu₂O Cubes, Octahedra, and Rhombic Dodecahedra. *J. Phys. Chem. C* **2018**, *122*, 13027-13033.

- (49) Hsieh, P.-L.; Naresh, G.; Huang, Y.-S.; Tsao, C.-W.; Hsu, Y.-J.; Chen, L.-J.; Huang, M. H., Shape-Tunable SrTiO₃ Crystals Revealing Facet-Dependent Optical and Photocatalytic Properties. *J. Phys. Chem. C* **2019**, *123*, 13664-13671.
- (50) Sun, Y.; Wang, W.; Qin, J.; Zhao, D.; Mao, B.; Xiao, Y.; Cao, M., Oxygen vacancy-rich mesoporous W₁₈O₄₉ nanobelts with ultrahigh initial Coulombic efficiency toward high-performance lithium storage. *Electrochim. Acta* **2016**, *187*, 329-339.
- (51) Drouilly, C.; Krafft, J.-M.; Averseng, F.; Casale, S.; Bazer-Bachi, D.; Chizallet, C.; Lecocq, V.; Vezin, H.; Lauron-Pernot, H.; Costentin, G., ZnO Oxygen Vacancies Formation and Filling Followed by in Situ Photoluminescence and in Situ EPR. *J. Phys. Chem. C* **2012**, *116*, 21297-21307.
- (52) Kaftelen, H.; Ocakoglu, K.; Thomann, R.; Tu, S.; Weber, S.; Erdem, E., EPR and photoluminescence spectroscopy studies on the defect structure of ZnO nanocrystals. *Phys. Rev. B* **2012**, *86*, 014113.
- (53) Jing, L.; Xu, Z.; Shang, J.; Sun, X.; Cai, W.; Guo, H., The preparation and characterization of ZnO ultrafine particles. *Mater. Sci. Eng., A* **2002**, *332*, 356-361.
- (54) Zhang, N.; Li, X.; Ye, H.; Chen, S.; Ju, H.; Liu, D.; Lin, Y.; Ye, W.; Wang, C.; Xu, Q.; Zhu, J.; Song, L.; Jiang, J.; Xiong, Y., Oxide Defect Engineering Enables to Couple Solar Energy into Oxygen Activation. *J. Am. Chem. Soc.* **2016**, *138*, 8928-8935.
- (55) Greiner, M. T.; Chai, L.; Helander, M. G.; Tang, W.-M.; Lu, Z.-H., Transition Metal Oxide Work Functions: The Influence of Cation Oxidation State and Oxygen Vacancies. *Adv. Funct. Mater.* **2012**, *22*, 4557-4568.
- (56) Xie, Y. P.; Liu, G.; Yin, L.; Cheng, H.-M., Crystal facet-dependent photocatalytic oxidation and reduction reactivity of monoclinic WO₃ for solar energy conversion. *J. Mater. Chem.* **2012**, *22*, 6746-6751.
- (57) Göpel, W.; Anderson, J. A.; Frankel, D.; Jaehnig, M.; Phillips, K.; Schäfer, J. A.; Rocker, G., Surface defects of TiO₂(110): A combined XPS, XAES AND ELS study. *Surf. Sci.* **1984**, *139*, 333-346.
- (58) Tokarz-Sobieraj, R.; Hermann, K.; Witko, M.; Blume, A.; Mestl, G.; Schlögl, R., Properties of oxygen sites at the MoO₃(010) surface: density functional theory cluster studies and photoemission experiments. *Surf. Sci.* **2001**, *489*, 107-125.
- (59) Knutsson, J. V.; Lehmann, S.; Hjort, M.; Lundgren, E.; Dick, K. A.; Timm, R.; Mikkelsen, A., Electronic Structure Changes Due to Crystal Phase Switching at the Atomic Scale Limit. *ACS Nano* **2017**, *11*, 10519-10528.
- (60) Hervieu, M., The Surface Science of Metal Oxides. By V. E. Henrich and P. A. Cox, Cambridge University Press. *Adv. Mater.* **1995**, *7*, 91-92.
- (61) Deb, S. K., Opportunities and challenges in science and technology of WO₃ for electrochromic and related applications. *Sol. Energy Mater. Sol. Cells* **2008**, *92*, 245-258.
- (62) Chatten, R.; Chadwick, A. V.; Rougier, A.; Lindan, P. J. D., The Oxygen Vacancy in Crystal Phases of WO₃. *J. Phys. Chem. B* **2005**, *109*, 3146-3156.
- (63) Liu, J.; Ke, J.; Li, D.; Sun, H.; Liang, P.; Duan, X.; Tian, W.; Tadé, M. O.; Liu, S.; Wang, S., Oxygen Vacancies in Shape Controlled Cu₂O/Reduced Graphene Oxide/In₂O₃ Hybrid for Promoted Photocatalytic Water Oxidation and Degradation of Environmental Pollutants. *ACS Appl. Mater. Interfaces* **2017**, *9*, 11678-11688.
- (64) Liao, L.; Zhang, Q.; Su, Z.; Zhao, Z.; Wang, Y.; Li, Y.; Lu, X.; Wei, D.; Feng, G.; Yu, Q.; Cai, X.; Zhao, J.; Ren, Z.; Fang, H.; Robles-Hernandez, F.; Baldelli, S.; Bao, J., Efficient solar water-splitting using a nanocrystalline CoO photocatalyst. *Nat. Nanotechnol.* **2013**, *9*, 69.

- (65) Liu, X.; Wang, F.; Wang, Q., Nanostructure-based WO₃ photoanodes for photoelectrochemical water splitting. *Phys. Chem. Chem. Phys.* **2012**, *14*, 7894-7911.
- (66) Wen, Z.; Wu, W.; Liu, Z.; Zhang, H.; Li, J.; Chen, J., Ultrahigh-efficiency photocatalysts based on mesoporous Pt–WO₃ nanohybrids. *Phys. Chem. Chem. Phys.* **2013**, *15*, 6773-6778.
- (67) Berak, J. M.; Sienko, M. J., Effect of oxygen-deficiency on electrical transport properties of tungsten trioxide crystals. *J. Solid State Chem.* **1970**, *2*, 109-133.
- (68) Baroni, S.; Resta, R., Ab initio calculation of the macroscopic dielectric constant in silicon. *Phys. Rev. B* **1986**, *33*, 7017-7021.
- (69) Ping, Y.; Galli, G., Optimizing the Band Edges of Tungsten Trioxide for Water Oxidation: A First-Principles Study. *J. Phys. Chem. C* **2014**, *118*, 6019-6028.
- (70) Heyd, J.; Scuseria, G. E.; Ernzerhof, M., Hybrid functionals based on a screened Coulomb potential. *J. Chem. Phys.* **2003**, *118*, 8207-8215.
- (71) Heyd, J.; Scuseria, G. E.; Ernzerhof, M., Erratum: “Hybrid functionals based on a screened Coulomb potential” [J. Chem. Phys. 118, 8207 (2003)]. *J. Chem. Phys.* **2006**, *124*, 219906.
- (72) Perdew, J. P.; Burke, K.; Ernzerhof, M., Generalized Gradient Approximation Made Simple. *Phys. Rev. Lett.* **1996**, *77*, 3865-3868.
- (73) Dudarev, S. L.; Botton, G. A.; Savrasov, S. Y.; Humphreys, C. J.; Sutton, A. P., Electron-energy-loss spectra and the structural stability of nickel oxide: An LSDA+U study. *Phys. Rev. B* **1998**, *57*, 1505-1509.
- (74) Kresse, G.; Furthmüller, J., Efficient iterative schemes for ab initio total-energy calculations using a plane-wave basis set. *Phys. Rev. B* **1996**, *54*, 11169-11186.

Table of Contents



The crystal phase of tungsten oxide (WO₃) nanoplates has been modulated with a simple and mild trioctylphosphine-trioctylphosphine oxide treatment. The induced oxygen vacancies in WO₃ nanoplates induce the monoclinic to pseudo-cubic phase transition and the reformation of band structure, which enables stable photocatalytic hydrogen evolution without co-catalyst.